TIP LEAKAGE FLOW AND ITS IMPLICATION ON THE ACOUSTIC SIGNATURE OF A LOW-SPEED FAN

Aurélien MARSAN[1], Dominic LALLIER-DANIELS[1], Marlène SANJOSÉ[1], Adrien MANN[2], Stéphane MOREAU[1]

[1] *Université de Sherbrooke, Mechanical Engineering departement, Québec, Canada.*

[2] *EXA Corporation.*

SUMMARY

The tip leakage flow and its impact on the far-field noise is studied on the Rotating Controlled-Diffusion Blade (RCDB) low-speed fan. Three numerical setups aiming at describing the flow through the RCDB fan test rig are compared at the nominal operating point. All numerical setups predict the overall performance of the fan well. However, major differences are observed that depend on the size of the finest cell and the type of boundary condition that is used at the outlet of the computational domain. A detection technique of coherent flow structures by a modal analysis is applied at a near-stall operating point where tip leakage flow becomes significant. It reveals the modal structure of the tip leakage flow and highlights the existence of circumferential rotating modes at the near-stall flow condition. These modes explain the tonal acoustic signature of the fan.

INTRODUCTION

Fans and blowers are omnipresent in daily life. They are used in large scale Heating, Ventilation and Air-Conditioning (HVAC) systems, automotive cooling systems as well as small scale systems such as electronic cooling systems for home computers. They represent as many sources of noise disturbances. Meanwhile, the health impacts of environmental noise are fast becoming a growing concern. A recent report from the World Health Organization concludes that « If negative effects on sleep are to be avoided the equivalent sound pressure level should not exceed 30 dBA indoors for continuous noise ». This is a challenge for fan and blower manufacturers. A new generation of both efficient and quiet air moving systems is needed. For that purpose, a better understanding of the noise generation mechanisms in low-speed fans and blowers is required.

Within this scope, a consortium named Ultra High-Efficiency Quiet (UHEQ) Fans [1, 2] has been established between Michigan State University (MSU), University of Notre Dame (ND) and Univer-

sité de Sherbrooke (UdeS) to study and reduce aerodynamic losses and noise in low-speed fans. The first phase of this consortium from 2010 to 2015 focused on the collection of experimental data sets. The present phase of the UHEQ consortium aims at using advanced numerical tools together with the available experimental database in order to give a strong understanding of the noise generation mechanisms in blowers and fans. The final objective is to develop a fast and accurate analytical tool for pre-design, dedicated to the fan noise prediction.

The present paper investigates the influence of the tip leakage flow on the noise radiation of the low-speed RCDB axial fan using numerical simulations. First, three numerical setups are compared to the available experimental results at the nominal operating point (OC1). The comparison shows the influence of the numerical parameters of the Lattice-Boltzmann method as implemented in PowerFLOW. The best setup is retained for the second part of the paper where the analysis focuses on the tip leakage flow and a modal detection technique is applied in order to detect the coherent structures in the tip leakage flow.

ROTATING CONTROLLED-DIFFUSION BLADE

Experimental setup

The fan investigated in this study, termed Rotating Controlled-Diffusion Blade (RCDB), is a research fan that has been subject to an extensive experimental investigation using the Axial Fan Research and Development (AFRD) test facility at MSU [1]. The AFRD facility consists in a 3x3x2 m large plenum, the test fan being mounted in an opening on the ceiling wall. The hub and tip radii are 240 mm and 366 mm, respectively. The diameter of the duct is 740 mm, and there is a 4 mm annular tip clearance with the shroud surface. The design of the blade is based on the same controlled diffusion (CD) profile from hub to tip and on the use of a generalized radial equilibrium technique described in [3]. The blade span is 135.2 mm and the chord is constant equal to 133.9 mm along the whole span. The RCDB was designed to be modular and is able to accommodate from 2 to 9 blades. The design flow rate of the fan is 2.31 kg/s and the design rotational speed is 437 RPM. This corresponds to a geometric angle of attack of 8° at mid-span (taken from the chord line) and an upstream relative velocity of 16.25 m/s. The Reynolds number based on the chord length is then equal to 1.5×10^5 at mid-span and this operating condition has been intensively studied for the stationnary CD airfoil. This operating condition is refered as (OC1) and it allows to assess the rotational effects.

Three operating points covering the entire stable operating range are considered in the present work: (OC1) is the nominal operating condition and has been experimentally studied by Neal and Cawood [4, 5]; (OC3) is close to free-flow operating condition and has been experimentally studied by Cawood, Davoudi and Barrent [5, 6, 7]; (OC5) is a near-stall operating condition which has been experimentally studied by Davoudi and Barrent [6, 7].

Available experimental data from the AFRD facility include wall-pressure measurements on the fan blades along the chord for several radial positions. Hot-wire anemometry and PIV measurements were also conducted to provide an in-depth description of the flowfield encountered downstream of the fan. More recently, aeroacoustic measurements were also carried out within the non-anechoic AFRD flow facility, at operating conditions (OC3) and (OC5) only. The use of an auxiliary fan was required to reach the negative pressure rise at (OC1) compromising any assessment of self noise for this operating point.

Complete details about the experimental test rig and the available experimental data are given in [1].

Numerical setup

For the purposes of this study, the 3-blade RCDB configuration within the full AFRD facility was simulated using a V-LES Lattice-Boltzmann method (LBM) as implemented in the PowerFLOW solver to further investigate the entire flowfield around the fan. This approach is naturally transient and compressible, providing direct insight into aerodynamic mechanisms responsible for the acoustic sources but also into acoustic propagation in the test-rig [8, 9, 10, 11].

The simulation case is based on a previous study by Pérot et al. [10] of the RCDB geometry. The numerical simulation for the RCDB test fan was meant to mimic the experimental conditions of the AFRD facility where the fan is mounted on the ceiling of a large plenum chamber, with the air being taken from the surrounding room where the fluid is at rest.

The simulation domain, shown in Fig.1(a), is 130 m wide, 130 m long and 65 m high. The side walls and ceiling have static pressure freeflow boundary conditions imposed to represent a large quiescent room, whilst a solid wall condition is imposed to represent the plenum surfaces on the floor surface. The test plenum inlet is centered in the simulation domain. A wireframe view of the plenum volume is shown in Fig 1(b), with the fan and its bellmouth inlet visible at the top of the plenum. The flow rate through the system is regulated by the outlet boundary condition at the exit surface of the outlet duct. Two outlet conditions have been used : (a) a mass flow boundary condition and (b) a constant velocity outlet boundary condition. The mass flow boundary condition is indeed shown to be a reflective condition that can generate spurious acoustic modes [12], and the constant velocity outlet boundary condition has then been tested in the present study.

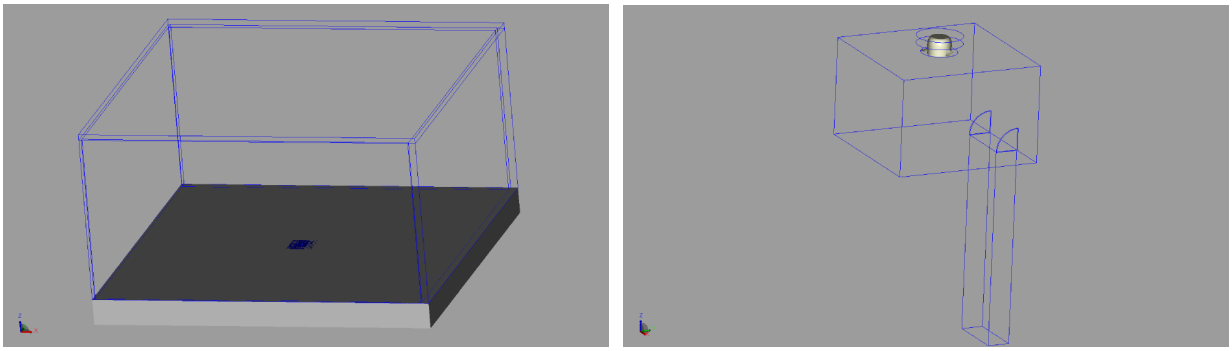

(a) Simulation domain (b) Plenum volume

Figure 1: View of the RCDB computational domain.

Three separate grids have been used. The first, shown in Fig. 2(a), has been used for the numerical *Setup 1*. The smallest voxel size is 1 mm around the rotor blades. Voxel size is then 2 mm in the rest of the rotor domain. In order to decrease the amount of disk space required for the storage of the computational results, PowerFLOW allows to extract the volume data on a measurement grid with a voxel size multiplied by 2 compared to the mesh used for the computation. This option has been used for all the numerical setups presented here and then the cell size in the measurement grid shown in Fig. 2(a) is twice that of the mesh used for the computation. The second mesh, shown in Fig. 2(b), has been used for the second numerical *Setup 2*. 1 mm voxels are now used all over the blade-to-blade passage and along the hub surface. The objective was to better capture the details of the boundary-layers growth and the propagation of the tip leakage flow. The third mesh, shown in Fig. 2(c), has been used for the numerical *Setup 3*. The voxel size is 0.5 mm voxels around the fan blades. This corresponds to a resolution of 1480 voxels across the fan diameter, which is a very fine resolution according to the Best Practice for fans of Exa Corporation, that recommends a resolution of 1200 voxels per diameter at least in order to capture accurately the details of the flow through a

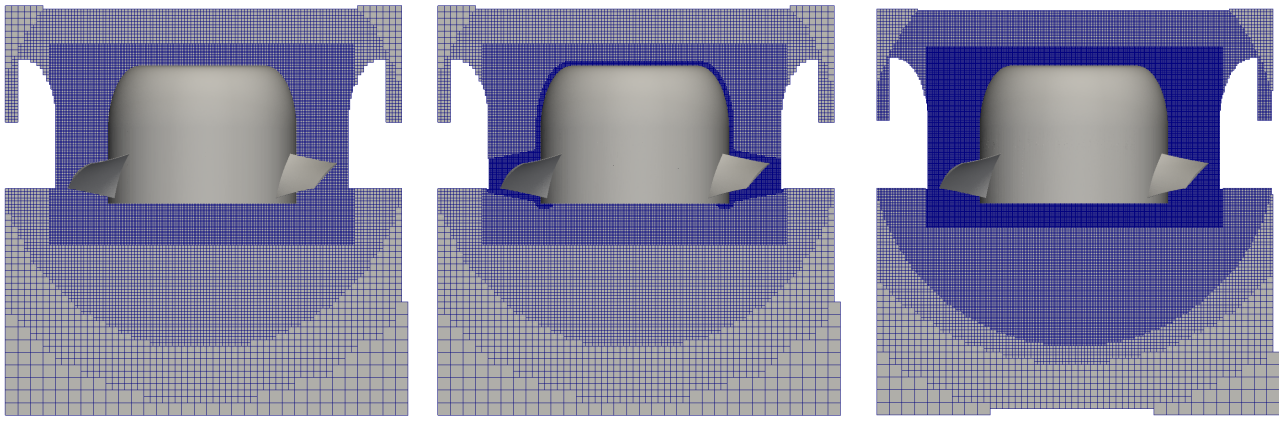

(a) *Setup 1* (b) *Setup 2* (c) *Setup 3*

Figure 2: View of the measurement grids for the different setups. Cell size is twice as the computational mesh.

low-speed fan. 1 mm voxels are then used in the blade to blade passage and in the vicinity of the fan for the third mesh.

All the numerical setups have been run with the real Mach number value of 0,047. The outlet boundary condition is a mass flow boundary condition for *Setup 1* and *Setup 3* whereas the velocity outlet boundary condition has been used for *Setup 2*. The *Setup 1* has been run for 40 rotations. The *Setup 2* has been run for 30 rotations. The *Setup 3* has been run for only 2 rotations and will not be considered in the further statistical analysis given the lack of simulation time.

INFLUENCE OF THE NUMERICAL SETUP

Performance

Fig. 3 shows the experimental performance characteristic curve together with the three operating points that have been numerically computed. Operating condition (OC1) has been computed with all the numerical setups from 1 to 3. (OC3) and (OC5) have been computed with *Setup 1* and *Setup 2*. A good agreement can be observed between the numerical predictions and the experimental measurements. In particular, the performance at operating condition (OC1) is well predicted whatever the numerical setup is. Therefore, the Lattice-Boltzmann method as implemented in PowerFLOW predicts the global performance and the acoustics of the RCDB fan well.

Pressure coefficient

Fig. 4 shows the wall-pressure coefficient distribution $C_p = \frac{p-p_{ref}}{0.5\rho U_{ref}^2}$ at mid-span and at (OC1) for the three numerical setups. Experimental data from Neal [4] are also shown. The C_p coefficient is computed from the mean pressure value over the last rotation for the *Setup 1* and *Setup 2*. It is computed from the last time step of the computation only for *Setup 3*, which explains the oscillation of the surface pressure that are seen on the suction side in the second half of the chord in green.

All numerical setups properly capture the wall-pressure distribution on the pressure side until 90% of the chord length, but only *Setup 3* describes the C_p until the trailing edge well. *Setup 1* and *Setup 2* predict a plateau and a pressure jump around the trailing edge which is not observed in the experimental results. On the suction side, a laminar separation bubble exists as suggested by the hump and plateau in the experimental curve in the first 10% of chord [13]. This laminar separation bubble is well known

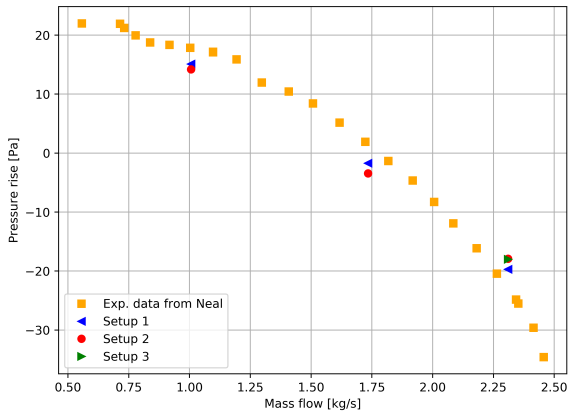

Figure 3: Performance characteristic curve for the RCDB fan (3-blades).

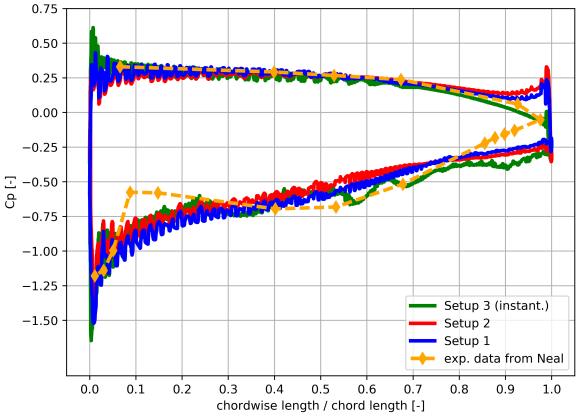

Figure 4: Mean C_p distribution at mid-span for (OC1).

on the CD airfoil at this operating condition and is expected as well in the RCDB. It controls the development of the boundary layer as it triggers the transition from laminar to turbulent. For the CD airfoil using the PowerFLOW solver v4.3b, the recirculation bubble was captured with a mesh size at the wall of 48 µm needed to resolve the initial strong shear at the leading-edge [14]. All the three numerical setups equally fail at capturing this laminar recirculation bubble. As a consequence, no turbulent structures are generated and the boundary layer grows more laminar than in the experiments yielding a quasi flow separation at the trailing edge and a much thicker wake, as shown in the next section.

Wake velocity profiles

The u-component of the velocity is computed by the projection of the relative velocity in the direction of the upstream velocity. This coordinate system was introduced by Neal [4] as it allows a direct comparison with the components of the velocity measured downstream of the isolated CD airfoil mounted in a wind tunnel.

Fig. 5 shows the mean of the u-component of the velocity in the near wake at $z/c = 5\%$ downstream of the trailing edge and at midspan where z is the axial coordinate. The zero of the $r\theta$ axis corresponds to the location of the trailing edge, the suction side being located on the $r\theta < 0$ side and the pressure side on the $r\theta > 0$ side. As seen previously for the C_p the numerical cases mostly differ from the experiments on the suction side of the wake. All setups overpredict the depth and the width of the blade. The finest *Setup 3* is the closest to the experimental results which suggest that this setup should be run more that the actual 2 rotations. The finest voxel size may also be further decreased.

Fig. 6 plots the evolution of the velocity deficit as a function of the axial distance from the fan trailing edge. As already observed, the velocity deficit is overpredicted by all the numerical setups. The decrease of the velocity deficit with the distance to the trailing edge is also different between the three setups. *Setup 1* and *Setup 2* have the smallest rate of decrease and the velocity deficit remains too large even at $z = c = 0.50$. The decrease rate is higher with the finest *Setup 3* but the wake still remains too deep until $z/c = 50\%$.

Circumferential map of the velocity

Fig. 7 shows the instantaneous map of the u-component of the velocity around one blade at mid-span and operating condition (OC1). For all the numerical setups the boundary layer separates near the trailing edge and on the suction side. Only in the *Setup 3* the laminar separation bubble can be hardly

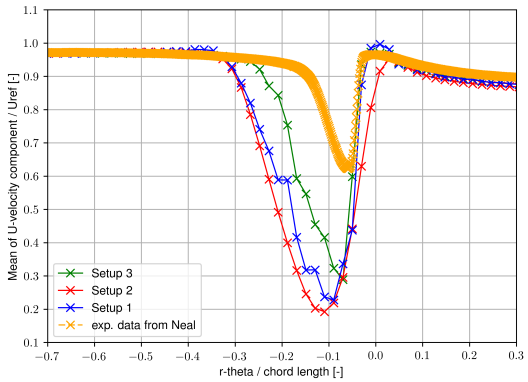

Figure 5: $z/c = 5\%$, mean u-component of the velocity in the wake, mid-span.

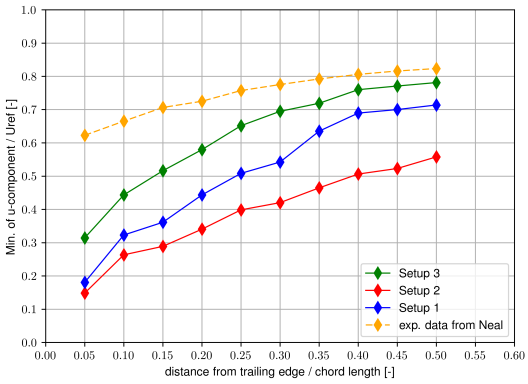

Figure 6: Velocity deficit at mid-span.

seen. It results in a vortex shedding that increases the mixing rate between the external flow and the boundary layer and decreases the size of the boundary layer separation at the trailing-edge. The insufficient resolution of the boundary layer on the blade suction side in the numerical setups results in the too large wakes seen in the previous section. V-LES may not be suitable in this particular case for capturing the transition to the turbulence on the suction side through a laminar recirculation bubble. Further investigations are needed and may be inspired by the previous numerical work on the CD airfoil using the same numerical solver, which has led to a perfect match between the numerically predicted C_p and the experimental measurements only provided a mesh resolution fine enough to capture the recirculation bubble properly [14, 15].

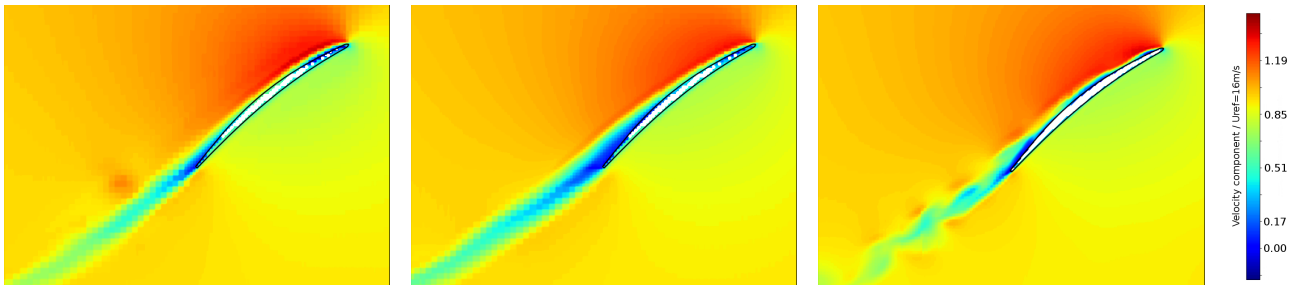

(a) Setup 1 (b) Setup 2 (c) Setup 3

Figure 7: Instantaneous maps of the u-component of the velocity at mid-span.

Tip leakage flow structure

The final aerodynamic comparison between all the setups is made on the basis of the tip leakage flow structure that will be analyzed later by means of a modal technique. Iso-surface of the Q-criterion colored by the value of the axial velocity is shown in Fig. 8. Only the iso-surfaces upper than 25% of the passage height are shown, and then no structures near the hub are plotted.

All numerical setups predict globally the same flow structure with a tip-leakage vortex (labeled as A in Fig. 8(a)) being shed from the blade leading edge, then propagating toward downstream and across the blade-to-blade passage. A vortex of smaller size (labeled as B) originates from the main tip leakage vortex and passes just downstream of the trailing edge of the adjacent blade, before merging with the main tip leakage vortex of the adjacent blade (location labeled as C). The main difference between the numerical setups is that smaller structures are present when the mesh is refined. The smaller structures

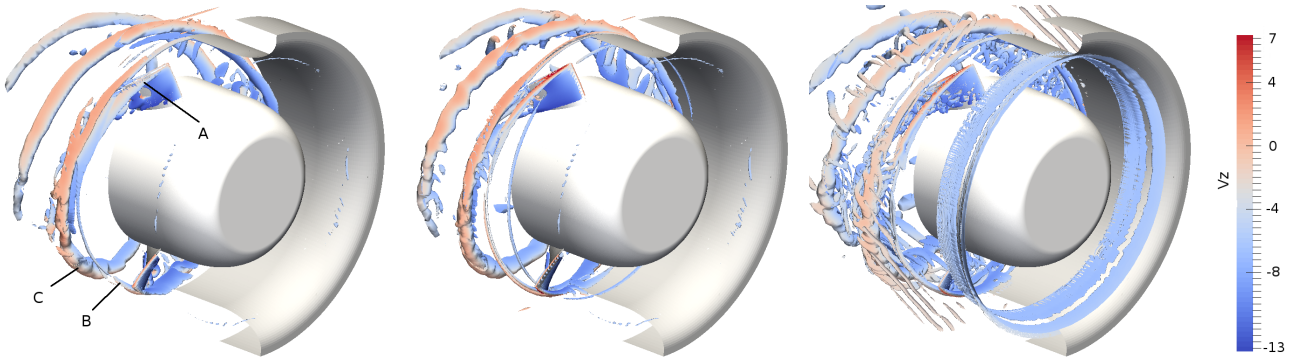

(a) Setup 1 (b) Setup 2 (c) Setup 3

Figure 8: Contours of Q-criterion $= 8 \cdot 10^3$ *at (OC1), colored by axial velocity (negative toward downstream).*

are predicted with the numerical *Setup 3* which has the smaller finest voxel size.

Upstream acoustic pressure

Fig. 9(a) shows the acoustic spectra as recorded 0.6 m upstream of the fan hub along the rotational axis for the operating conditions (OC1) and the numerical *Setups 1-2*. *Setup 3* is not considered in this analysis given the too short simulation time. The plot shows the power spectral density (PSD) of the pressure signals as computed by Welch's periodogram method using a Hanning window. The pressure signal is 2 seconds long and it is sampled at a rate of 9478 Hz. The windows are 1 second length with 0.75 second overlap.

In Fig. 9(a), several peaks are predicted at 21 Hz, 54 Hz, 63 Hz, 86 Hz, 95 Hz and 108 Hz with the *Setup 1*. The peaks at 21 Hz, 63 Hz and 86 Hz are close to the blade passing frequency (BPF=21.85 Hz) and its second and third harmonics respectively (65.55 Hz and 87.4 Hz). In order to understand the origin of the other peaks, the Helmholtz equation is solved on the whole set-up using ASVP developed at Cerfacs [16]. This analysis has found several acoustic resonant modes of the RCDB plenum configuration at the frequencies 10 Hz, 39 Hz, 58 Hz, 79 Hz, 81 Hz, 99 Hz, 112 Hz, 113 Hz, 114 Hz, 118 Hz, 122 Hz and 127 Hz. The peaks at 54 Hz, 95 Hz and 108 Hz are then close to a natural frequency of the installation. There is a coupling between the blade passing frequency and the natural frequency of the installation in *Setup 1*. With *Setup 2* that uses a constant velocity outlet boundary condition, all the peaks disappear and what was a highly tonal spectra becomes broadband as was reported experimentally for this operating condition.

As explained previously, no experimental data about the RCDB self noise at (OC1) are available given the use of an auxiliary fan to reach that operating condition, but such experimental data are available at (OC3) and (OC5). A special beamforming technique has been used by Davoudi et al. [6, 2] to account for the non-anechoic environment and evaluate the noise radiated by the RCDB fan. This beamforming technique has been replicated numerically and the comparison between the experiments and the *Setup 2* is shown in Fig. 10. Only frequencies higher than 200 Hz are shown. Due to the reflective nature of the test environment, a high-pass filter with a threshold of 200 Hz was applied and the spectra below this frequency can not be compared. The sharp peaks visible in the experimental data are artefacts of the experimental setup, not related to aeroacoustic mechanisms and should be ignored in the present analysis. A good agreement between the numerical prediction of *Setup 2* and the experimental data is obtained up to 1 kHz at both operating points (OC3) and (OC5). Then the cutoff frequency associated to the numerical setup is reached and the numerical curve flattens.

For the rest of the paper, a detailled analysis of the structure of the tip leakage flow structure and its

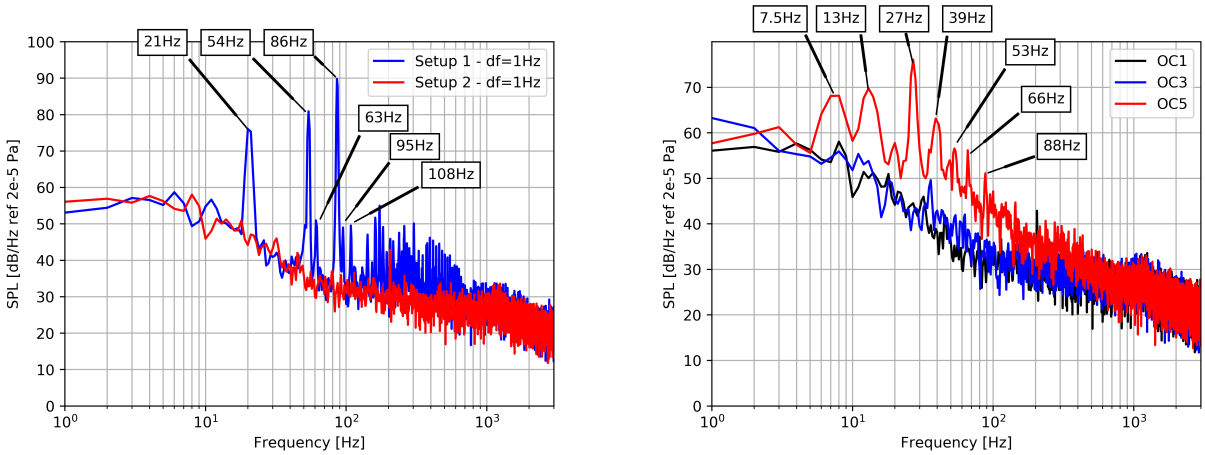

(a) (OC1). All setups. (b) (OC1)-(OC3)-(OC5). *Setup 2*.

Figure 9: Upstream sound pressure spectra. Numerical predictions only.

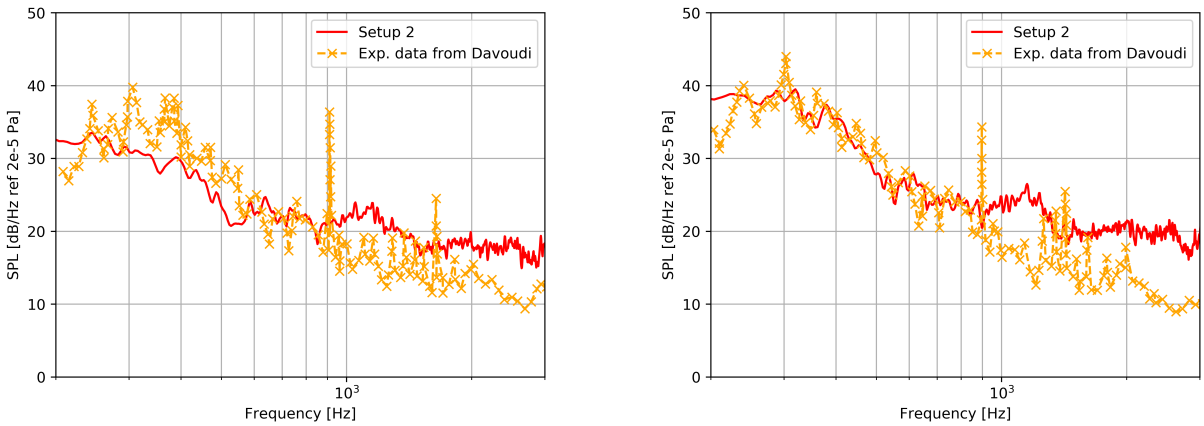

(a) (OC3) (b) (OC5)

Figure 10: Comparison of Setup 2 *and experimental data from Davoudi [2] for the upstream sound pressure spectra computed with beamforming technique.*

implication on the acoustic signature of the fan is performed based on the results obtained with *Setup 2*, which compares well with the experimental upstream acoustic radiation.

TIP LEAKAGE FLOW NOISE

Evolution of the noise from (OC1) to (OC5)

Fig. 9(b) shows the spectra computed from the numerical simulations at (OC1), (OC3) and (OC5). The parameters of the Welch's method are the same as previously given, providing a frequency resolution of 1 Hz. The radiated noise is typically broadband at (OC1) and (OC3) whereas tones and humps emerge at (OC5). The frequencies of the tones and humps are indicated in the figure. The peak at 7.5 Hz is close to the rotational frequency of the fan (7.28 Hz). The peaks at 66 Hz and 88 Hz are close to the second and third harmonics of the BPF. The peak at 39 Hz correspond to a natural frequency of the system as predicted by the aforementionned 3D Helmholtz solver. The peaks at 13 Hz, 27 Hz and

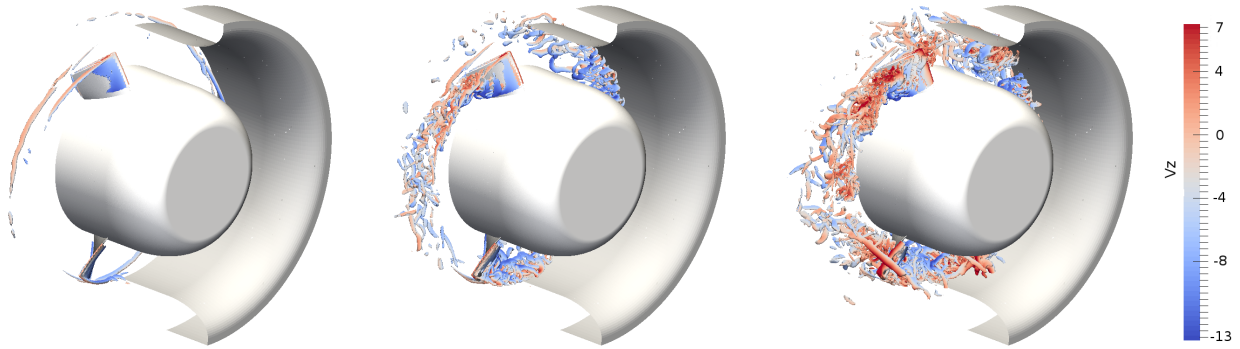

(a) Operating condition (OC1) (b) Operating condition (OC3) (c) Operating condition (OC5)

Figure 11: Contours of Q-criterion $= 10^5$*,* Setup 2.

53 Hz correspond to neither a natural frequency of the system, nor an harmonic of the BPF.

Fig. 11 shows iso-surface of the Q-criterion colored by the value of the axial velocity, in the same manner as in Fig. 8. (OC5) the flow is fully detached from the blade tip and propagates in the rotor passage until the adjacent blade. Such an interaction has been shown to be the source of sub-harmonic humps [17, 12, 18].

Modal analysis at (OC5)

A modal analysis is performed in order to better understand the different acoustic signatures and its link with the structure of the tip gap coherent flow structures. This method has been used by Zhu et al. [18], a supplementary wavelet analysis being introduced here in order to estimate the amplitude of the distortions caused by the detected structures. The method is based on the identification of the coherent flow structures as a superposition of rotating circumferential wave patterns superimposed on the base flow. The coherence function is used as a filter for the identification of coherent structures, which are then decomposed into rotating modes. These rotating modes rotate at speeds different from the rotor rotational speed and then interact with the blades, which results in the presence of typical narrowband humps in the acoustic signature of the fan, as observed for the present test case at the near-stall operating condition (OC5).

In the present test case, numerical circumferential arrays have been setup at seven radial positions varying from just under the tip of the blades (R=365 mm) to a radial position of 341 mm, and at a total of 11 axial positions at each radius from the rotor inlet to the rotor outlet. Fig. 14(a) shows one of the 90 column of arrays that are distributed over the whole circumference of the fan. In the figure, the color of the probes varies with their axial and radial positions. Each color corresponds to a single radius, and varies from light to dark together with the axial position of the probe. Given the number of columns the circumferential resolution is 4 degrees. The pressure signal is extracted from the simulation data in the rotating reference frame.

Fig. 12 illustrates the identification procedure that is made on the basis of the coherence and the cross-spectral density for a particular pair of probes. First, a threeshold is applied, and only the frequency range where the coherence value is above 0.7 (dashed red line in the upper figure) is considered for the analysis. In this frequency range, a strong linearity of the cross-spectral density phase is observed (see the bottom figure). The azimuthal mode order m is obtained as $m = \gamma_{xy}/\theta_{xy}$, where θ_{xy} is the azimuthal spacing between the probes and γ_{xy} is the phase of the cross-spectral density. Then, the rotational speed of the azimuthal mode is computed from the value of the frequency f and the order m as $n_{mod}/n = (2\pi f)/(m \times n)$ where n is the rotational speed of the rotor.

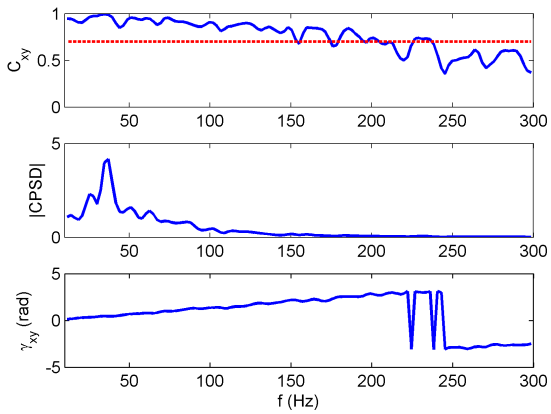

Figure 12: Plots for a pair of probes: cross-spectral coherence level (top), cross-spectral density amplitude (middle) and phase lag (bottom).

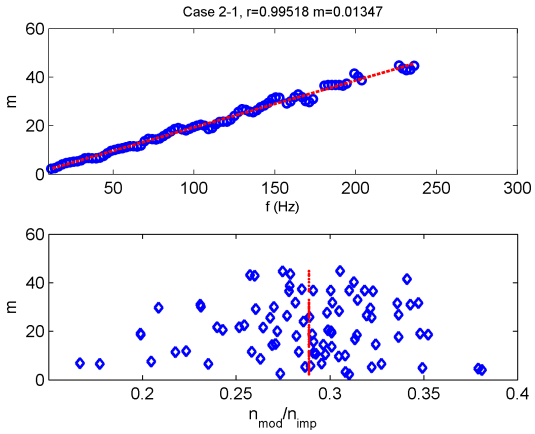

Figure 13: Characteristics of the modes identified as a result of the correlation analysis for the same pair of probes as in Fig. 12.

As a result, Fig. 13 plots the orders of the modes as a function of the frequency (top) and as a function of their rotational velocity (bottom), for the same pair of probes as used in Fig. 12. The dashed line in the upper diagram highlights the linear trend of the mode order as a function of frequency, which is a consequence of the linear trend of the phase. The dashed line in the bottom diagram corresponds to the unique modal velocity computed from the slope of the linear trend. The rotational velocity of the modes are spread around this mean value.

By extending this process to several radial and axial positions, a spatial analysis of the modes present in the flow is carried out and a more complete representation of the coherent modes in the tip region is achieved. The order of the modes detected in the tip region of the blades as well as their rotational velocity are shown in Fig. 14. In each plot, each color corresponds to a single radius and goes from light to dark from the rotor inlet to the rotor outlet, as shown in Fig. 14(a). Fig. 14(b) plots the amount of coherent flow structures that are detected as a function of their azimutal order m. Fig. 14(c) plots the amount of coherent flow structures that are detected as a function of their rotational speed. Finally, Fig. 14(d) plots the amount of coherent flow structures that are detected as a function of their interaction frequency with the rotor blades f_{int}. The acoustic spectra (Fig. 9(b) OC5) is recalled with the black line whose levels are provided on the right scale. The interaction frequency of a rotating azimutal mode is computed from its azimuthal order m, its rotational velocity relative to the rotor blades $n_{mod} - n$ and the number of blades of the rotor B according to $m \times (n_{mod} - n)/LCM(m, B)$ where LCM refers to the least common multiple number.

The coherent modes have an order up to 60. The most frequently encountered mode orders are between 6 to 8, indicating that there is a predominance of structures that span one half to one third of a blade passage. These modes rotate at a velocity equal approximately to 30% of the rotational speed of the fan. All the radius that have been investigated contribute equally to the number of detected events. Then these modes are detected in all the upper part of the rotor passage, and not only in the vicinity of the shroud. The comparison of the relative strength of the detected events with the upstream acoustic spectra shows that the main peak at about 30 Hz in the acoustic spectra is related with dominant coherent structures that are detected by the technique and interact with the rotor blade at almost the same frequency. Again, all the radius contribute equally to the strength of interaction between the detected modes and the blades.

Finally, structures in the vortical field around the RCDB fan blades the rotational velocity of which corresponds to the modal velocities of the identified modes can be identified in the flow by filtering the λ_2 field as shown in Fig. 15(a). This figure shows the filtered vortical field to include only the

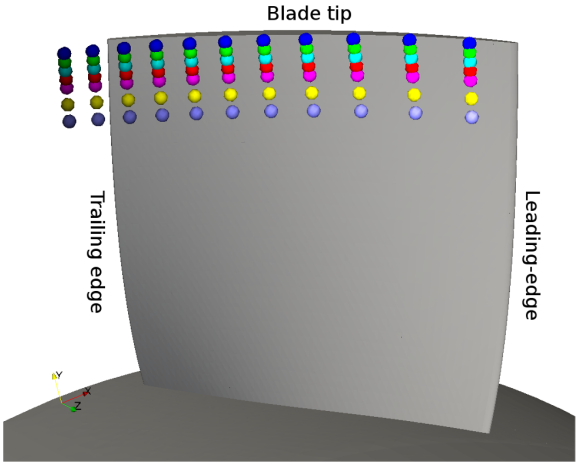

(a) View of one of the columns of the circumferential array of probes.

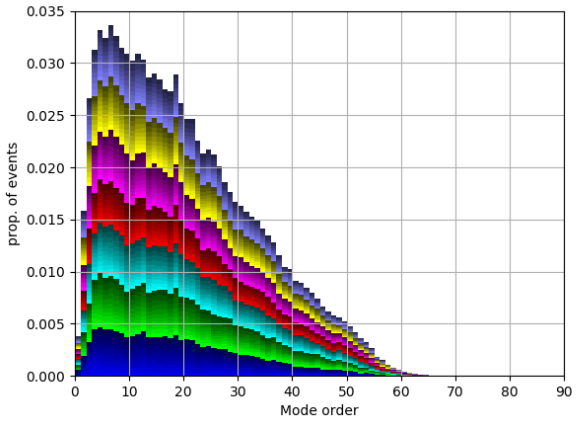

(b) Mode order of detected events

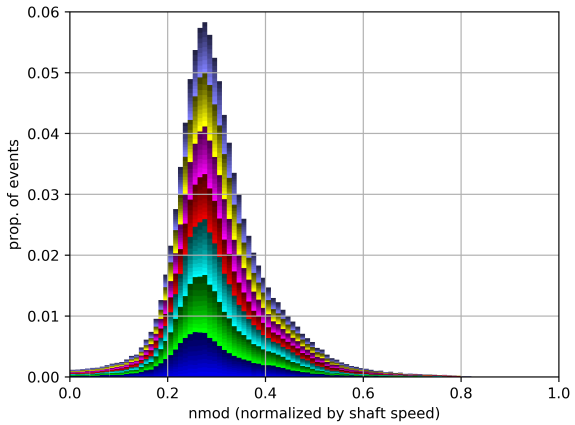

(c) Dimensionless rotational speed of detected events

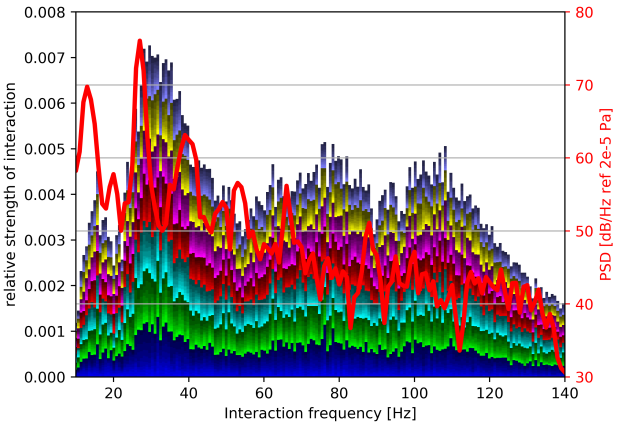

(d) Relative strength of the detected events as a function of the interaction frequencies. Upstream acoustic spectra in black.

Figure 14: Modal identification near the shroud, (OC5), Setup 2.

vortical structures exhibiting rotational velocities such as $0.1 \leq n_{mod}/n \leq 0.5$. Further filtering the pressure field in certain frequency bands and retaining only the structures associated with a certain mode order allows to highlight the pressure modes associated with the coherent structure field from Fig. 15(a). This additional filtering step is shown in Figs. 15(b) and 15(c) for the 90-110 Hz and 160-180 Hz frequency bands respectively, corresponding to mode orders 20 and 30, respectively. The modal patterns for each frequency band appear to correspond rather well to the expected mode orders. This confirms the presence of coherent modes in the flow, and comforts the results of the correlation analysis so far by linking the predicted modal characteristics to their actual occurrence in the flowfield. The coherent structures spread over the upper half of the rotor passage which is consistent with the observation that all radius in Fig.14 contribute equally to the number of detected events.

This modal analysis technique gives a precious insight into the behavior of the tip leakage flow field and its implication in the acoustic signature of the spectra. The same analysis should be performed on the *Setup 3* once the convergence reached, as the refined flow structures may provide more defined interactions at specific mode orders.

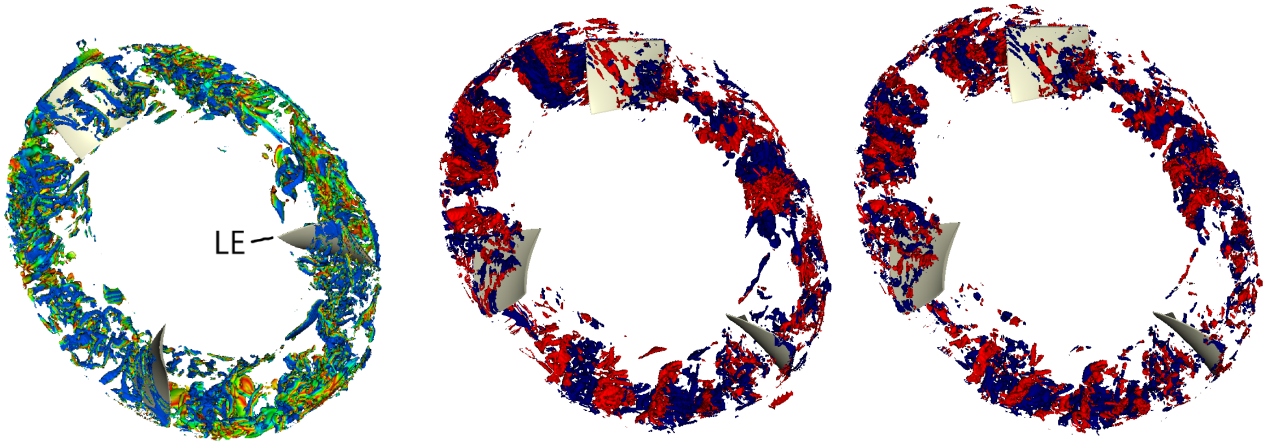

(a) (b) 90-110 Hz (c) 160-180 Hz

Figure 15: Filtered instantaneous vortical field at (OC5).

CONCLUSIONS AND OUTLOOK

Several LBM simulations have been successfully achieved on the RCDB fan which is the benchmark low-speed fan for the Ultra High-Efficiency Quiet (UHEQ) Fans consortium. All numerical setups predict the global performance and the acoustics of the RCDB fan well.

A detailed flow analysis has been achieved at a flow condition that has been previously studied intensively on the stationary CD airfoil. Differences are observed depending on the outlet boundary condition: a tonal acoustic signature is predicted with an imposed mass flow as outlet boundary condition whereas the signature is broadband with a constant velocity. This is attributed to the reflective nature of the mass flow boundary condition. Regarding the finest voxel size, all the setup equally fail at predicting the laminar recirculation bubble on the suction side of the blades. The finest setup with a smallest voxel size of 0.5 mm provides the best agrement with the experiments for the loading and wake development. Unfortunately the too short simulation time available was unsufficient for the acoustic analysis. For this reason, *Setup 2* was retained the acoustic analysis.

A modal detection technique of coherent flow structures has revealed the modal structure of the tip leakage flow as predicted by the numerical simulations. Rotating circumferential modes are found for the near-stall operation condition. They explain the tonal acoustic footprint that is predicted at this particular operating condition whereas the acoustic radiation of the fan is broadband at higher mass flow where no rotating modes can be identified in the flow field.

A valuable insight about the implication of the tip gap flow on the acoustic signature of the RCDB fan is given by this modal detection technique. It will be applied to the finest numerical setup once the convergence reached.

REFERENCES

[1] S. Moreau, K. Foss, and S. Morris. *A numerical and experimental test-bed for low-speed fans*. Proceedings of the Institution of Mechanical Engineers, Part A: Journal of Power and Energy, 230(5):456–466, **2016**.

[2] B. Davoudi, S. Morris, and J. Foss. *Aeroacoustic measurements for an axial fan in a non-*

anechoic environment. Measurement Science and Technology, 27(4):045003, **2016**.

[3] S. Moreau, G. Meauze, D. Lallier-Daniels, M. Sanjosé, J. De Laborderie, and Y. Mercadier. *Design of turbomachines by a novel full radial equilibrium method*. In *46th Symposium of Applied Aerodynamics, Aerodynamics of Rotating Bodies, Orléans*, **2011**.

[4] D. R. Neal. *The effects of rotation on the flow field over a controlled-diffusion airfoil*, **2010**.

[5] A. F. Cawood. *Surface pressure measurements on a rotating controlled diffusion blade*, **2012**.

[6] B. Davoudi. *Aeroacoustic and wake measurements on a rotating controlled diffusion blade*, **2014**.

[7] D. J. Barrent. *Controlled diffusion blade axial fan: Fluid mechanical mechanistic effects on fan performance*, **2015**.

[8] G. Bres, G. Pérot, and D. Freed. *Properties of the lattice-Boltzmann method for acoustics*. AIAA Paper, 3395:2009, **2009**.

[9] F. Perot, M-S. Moreau, S.and Kim, M. Henner, and D. R. Neal. *Direct aeroacoustics predictions of a low speed axial fan*. In *16th AIAA/CEAS aeroacoustics conference*, page 3887, **2010**.

[10] F. Pérot, S. Moreau, M-S. Kim, and D. R. Neal. *Investigation of the flow generated by an axial 3-blade fan*. In *13th ISROMAC Conference*, volume 82, **2010**.

[11] A. Mann, F. Pérot, M-S. Kim, D. Casalino, and E. Fares. *Advanced noise control fan direct aeroacoustics predictions using a Lattice-Boltzmann method*. AIAA paper, 2287:2012, **2012**.

[12] S. Moreau and M. Sanjose. *Sub-harmonic broadband humps and tip noise in low-speed ring fans*. The Journal of the Acoustical Society of America, 139(1):118–127, **2016**.

[13] S. Moreau, M. Henner, G. Iaccarino, M. Wang, and M. Roger. *Analysis of flow conditions in freejet experiments for studying airfoil self-noise*. AIAA journal, 41(10):1895–1905, **2003**.

[14] M. Sanjosé, S. Moreau, M.S. Kim, and F. Pérot. *Direct self-noise simulation of the installed controlled diffusion airfoil*. In *17th AIAA/CEAS aeroacoustics conference*, pages 05–08, **2011**.

[15] S. Moreau. *Symposium on the CD airfoil (20 years of collaboration)*. Available online. DOI:10.13140/RG.2.1.4512.4083, **2016**.

[16] F. Nicoud, L. Benoit, C. Sensiau, and T. Poinsot. *Acoustic modes in combustors with complex impedances and multidimensional active flames*. AIAA journal, 45(2):426, **2007**.

[17] S. Magne, S. Moreau, and A. Berry. *Subharmonic tonal noise from backflow vortices radiated by a low-speed ring fan in uniform inlet flow*. The Journal of the Acoustical Society of America, 137(1):228–237, **2015**.

[18] T. Zhu, D. Lallier-Daniels, M. Sanjosé, S. Moreau, and T. Carolus. *Rotating coherent flow structures as a source for narrowband tip clearance noise from axial fans*. Journal of Sound and Vibration, 417:198–215, **2018**.

ACKNOWLEDGEMENTS

EXA Corp. is gratefully acknowledged for providing PowerFlow licenses and support, and participating in fruitful discussions. The Centre for Research in Sustainable Aviation (CRSA) is also acknowledged for providing support to D. Lallier-Daniels. Some computations were made on the supercomputer Mammouth-MP2 from Université de Sherbrooke, managed by Calcul Québec and Compute Canada. Authors gratefully thank the Ultra High-Efficiency Quiet (UHEQ) Fans consortium whose funding allows the realization of this work.